



Tracy, Saoirse R. and Daly, Keith R. and Sturrock, Craig J. and Crout, Neil M.J. and Mooney, Sacha J. and Roose, Tiina (2015) Three-dimensional quantification of soil hydraulic properties using X-ray computed tomography and image-based modeling. *Water Resources Research*, 51 (2). pp. 1006-1022. ISSN 1944-7973

Access from the University of Nottingham repository:

http://eprints.nottingham.ac.uk/41200/1/141211_WRR_srtsjmkrd.pdf

Copyright and reuse:

The Nottingham ePrints service makes this work by researchers of the University of Nottingham available open access under the following conditions.

This article is made available under the University of Nottingham End User licence and may be reused according to the conditions of the licence. For more details see: http://eprints.nottingham.ac.uk/end_user_agreement.pdf

A note on versions:

The version presented here may differ from the published version or from the version of record. If you wish to cite this item you are advised to consult the publisher's version. Please see the repository url above for details on accessing the published version and note that access may require a subscription.

For more information, please contact eprints@nottingham.ac.uk

1 **Three dimensional quantification of soil hydraulic properties using X-ray Computed**
2 **Tomography and image based modelling**

3

4 **Author list:** Saoirse R. Tracy^{1§}, Keith R. Daly^{2§}, Craig J. Sturrock¹, Neil M. J. Crout¹, Sacha
5 J. Mooney¹, Tiina Roose^{2§}

6

7 **Author affiliations:**

8 ¹ School of Biosciences, University of Nottingham, Sutton Bonington Campus, Leicestershire,
9 LE12 5RD.

10 ² Bioengineering Sciences Research Group, Faculty of Engineering and Environment,
11 University of Southampton, University Road, SO17 1BJ.

12 [§]These authors are joint lead authors

13 [§] Corresponding author: Bioengineering Sciences Research Group, Faculty of Engineering and
14 Environment, University of Southampton, University Road, SO17 1BJ Southampton, United
15 Kingdom, email: l.roose@soton.ac.uk

16

17 **Key Points:**

- 18
- 19 • X-ray Computed Tomography is used to image water distribution in soil.
 - 20 • 3D Computed Tomography images are combined with image based modelling.
 - 21 • Unsaturated hydraulic conductivity and the water release characteristic are obtained.

22 **1. Abstract**

23 We demonstrate the application of a high-resolution X-ray Computed Tomography (CT)
24 method to quantify water distribution in soil pores under successive reductive drying. We focus
25 on the wet end of the water release characteristic (WRC) (0 to -75 kPa) to investigate changes
26 in soil water distribution in contrasting soil textures (sand and clay) and structures (sieved and
27 field structured), to determine the impact of soil structure on hydraulic behaviour. The 3D
28 structure of each soil was obtained from the CT images (at a 10 μm resolution). Stokes
29 equations for flow were solved computationally for each measured structure to estimate
30 hydraulic conductivity. The simulated values obtained compared extremely well with the
31 measured saturated hydraulic conductivity values. By considering different sample sizes we
32 were able to identify that the smallest possible representative sample size which is required to
33 determine a globally valid hydraulic conductivity.

34

35

36

37 **Keywords:** Matric potential; soil pores; water release characteristic; X-ray Computed
38 Tomography; image based homogenisation.

39

40 **Abbreviations:**

41 (3D) - 3-dimensional

42 (CT) - Computed Tomography

43 (ROI) - Region of interest

44 (WRC) – Water release characteristic

45 (WFP) – Water filled pores

46 (AFP) – Air filled pores

47 (REV) -Representative elementary volume

48

49 **Short title for page headings:** Three-dimensional quantification of soil hydraulic properties

50

Deleted:

51 2. Introduction

52 Understanding the dynamic nature of water movement through, and storage within, soil is of
53 fundamental importance for most of its functions. A more detailed knowledge of how soil
54 structure influences soil water distribution and subsequently availability to plants is needed to
55 inform soil management practices and thus contribute to efforts in increasing crop yields for
56 an expanding global population. However, to truly understand how water moves through soil
57 and is retained in soil pores whilst undergoing drying, non-destructive measurements of the
58 soil aggregate geometries and pore structure are needed. The use of X-ray Computed
59 Tomography (CT) to examine the 3D soil pore structure is rapidly gaining pace [*Helliwell et*
60 *al.*, 2014; *Mooney et al.*, 2012]. The ability to segment water from a greyscale CT image
61 remains challenging due to limitations in the phase separation achievable with regular detectors

62 in benchtop CT scanners. Segmentation of fluids in alternative porous media such as glass

63 beads has been previously described in the literature [*Haugen et al.*, 2014; *Iassonov et al.*,

64 2009]. However, due to the more complex, heterogeneous structure of soil and the associated

65 challenges faced during image acquisition this brings, these segmentation techniques cannot

66 always be readily applied to the segmentation of soil phases in X-ray CT images [*Houston et*

67 *al.*, 2013]. Yet, *Crestana et al.* [1985] highlighted the potential of CT for investigating water

68 movement through soil by quantifying the vertical and lateral water flows in 3D. By using dual

Deleted: well documented

Deleted: be easily

Deleted: using

73 energy tomography Rogasik *et al.* [1999] showed it is possible to quantify soil water, pore
74 space and bulk density. Mooney [2002], compared dry and moist samples and developed an
75 imaging method to separate water from the bulk soil in undisturbed soil cores albeit at a coarse
76 resolution (0.5 mm) using a medical CT scanner. Water flow characteristics were well matched
77 to macropore structure, with circa 90% of macropore space active in water transport in a sandy
78 clay texture, compared to circa 50% in the sandy loam soil. Wildenschild *et al.* [2005]
79 investigated multiphase flow processes and quantified drainage paths, showing that water is
80 preferentially lost from larger pores and the drainage of the remaining disconnected pores is
81 prevented. Since then Tippkotter *et al.* [2009] detected soil water in macropores and measured
82 water film thickness at a 20 μm resolution. They quantified the water without the use of contrast
83 enhancing agents or comparison of wet and dry scans. Partial volume effects make separating
84 boundaries between phases of interest a challenging task, due to the material of concern often
85 failing to fully fill a voxel [Ketcham and Carlson, 2001]. This can lead to individual voxels
86 being misclassified. However, as a microfocus system with a fine resolution was used in the
87 study, the impact of voxel misclassification is minimised [Clausnitzer and Hopmans, 2000].
88 The most recent advances in CT imaging technology now allow 3D non-destructive imaging
89 of soils at even higher resolutions, e.g. <3 μm spot size [Zappala *et al.*, 2013], allowing water
90 to be observed in smaller pores than previously considered.

Deleted: c.circa 0.5 mm

Formatted: Font: Not Italic

Deleted: similar to

Deleted: c.

Deleted: c.

Deleted: , they

Deleted: ed

Deleted:

91
92 The macroscopic scale flow in saturated and unsaturated porous media are often described
93 using a Darcy's law and Richards' equation [Hornung, 1997]. These equations are
94 parameterised by the unsaturated hydraulic conductivity and WRC. From a mathematical
95 perspective Darcy's law can be derived from the underlying Stokes equations using the method
96 of homogenization [Keller, 1980]. This approach has been applied to single porosity materials
97 [Hornung, 1997; Keller, 1980], double porosity materials [Arbogast and Lehr, 2006; Panfilov,

105 2000], and porous media containing voids or vugs [Arbogast and Lehr, 2006; Daly and Roose,
106 2014]. This method is based on the idea that the underlying porous structure is periodic, *i.e.*, it
107 is composed of a set of regular repeating units. By calculating the average fluid velocity for a
108 single representative unit volume due to a unit pressure drop, Darcy's law and the
109 representative hydraulic conductivity can be derived [Pavliotis and Stuart, 2008; Taylor *et al.*,
110 1970]. The mathematics underlying the WRC is less well established and homogenization
111 studies to date have assumed that the air water interface is known in advance [Taylor *et al.*,
112 1970].

113

114 Image based modelling can be loosely divided into two categories: pore network modelling
115 and direct simulation [Blunt, 2001; Blunt *et al.*, 2013]. The first of these, pore network
116 modelling, refers to the extraction of a representative network from the pore scale geometry
117 [Fatt, 1956] and has been widely used to predict averaged properties of packed spheres [Bryant
118 and Blunt, 1992; Bryant *et al.*, 1993b] and imaged porous media [Blunt, 2001; Blunt *et al.*,
119 2013; Bryant *et al.*, 1993a]. This technique is able to reproduce relative permeability curves
120 and water release characteristics. However, the pore network extraction results in a simplified
121 geometry which may neglect important pore scale phenomena. The alternative technique of
122 direct modelling involves solving equations directly on the imaged geometries. This technique
123 captures the detail of the pore scale geometry down to the resolution limit. The key
124 disadvantage is that modelling multiphase flow is demanding from a computational point of
125 view. Typically models of this type are based on Lattice Boltzman simulations of two fluids as
126 these are highly parallel and relatively easy to implement [Gao *et al.*, 2012; Ramstad *et al.*,
127 2010]. Other image based modelling studies in porous media include 3D image based
128 simulations of nutrient transport [Keyes *et al.*, 2013] and saturation based flow modelling of
129 water movement in 2-D image slices [Aravena *et al.*, 2014; Aravena *et al.*, 2011].

130

131 In this paper we demonstrate the application of a high resolution CT method to quantify water
132 distribution in soil pores under successive reductive drying. Using the structural geometries
133 from the CT images we apply the method of homogenization combined with direct image based
134 modelling to calculate the hydraulic conductivity across a range of matric potentials. This can
135 be seen as analogous to the measurement of a wetting phase relative permeability curve.
136 Specifically the question we aimed to answer is: what is the smallest possible Representative
137 Elementary Volume (REV) required to determine a hydraulic conductivity approximation
138 which is globally valid? In addition the soil moisture content is calculated directly from the CT
139 images at a range of different matric potentials and, hence, the WRC is derived. This approach
140 is chosen, rather than Lattice Boltzmann simulation, as it allows the WRC and hydraulic
141 conductivity to be calculated quickly without the need for time consuming two fluid
142 simulations. From the images we are able to obtain information on soil drainage in both
143 undisturbed field cores and sieved soils. This was used to accurately determine the impact of
144 soil structure on hydraulic behaviour.

145

146 3. **Materials and Methods**

147

148 3.1. *Sample preparation*

149 Soil was obtained from The University of Nottingham farm at Bunny, Nottinghamshire, UK
150 (52.52° N, 1.07° W). The soils used in this study were a Eutric Cambisol (Newport series,
151 loamy sand/sandy loam) and an Argillic Pelosol (Worcester series, clay loam). Particle size
152 analysis for the two soils was: 83% sand, 13% clay, 4% silt for the Newport series and 36%
153 sand, 33% clay, 31% silt for the Worcester series. Typical organic matter contents were 2.3%

Deleted: ¶

155 for the Newport series and 5.5% for the Worcester series [Mooney and Morris, 2008]. From
156 herein the two soil types are referred to as sand and clay soil. Loose soil was collected from
157 each site in sample bags and field cores (10 mm height, 10 mm diameter) were collected from
158 the immediate soil surfaces after any residues had been cleared. Four replicates were collected
159 for each soil type. Saturated hydraulic conductivity measurements of the field cores were
160 obtained via the standard laboratory method using a constant head device [Rowell, 1994].
161 Experimentally obtained hydraulic conductivity measurements were made for comparison with
162 the calculated values.

163

164 3.2. Measurement of the soil water release characteristic

165 In order to investigate the effect of drying on soil water distribution and soil structural changes
166 in 3D, a custom-built tension table was designed to hold the soil sample at a given matric
167 potential, whilst undergoing CT scanning. A small vacuum chamber was constructed
168 (Supplementary Figure 1), that contained a porous ceramic plate (Soil Moisture Corp, Santa
169 Barbara, CA, U.S.A) on top of which a field soil core was placed, with kaolin clay at the base
170 to ensure a good contact. The sample size was kept small to ensure high resolution scanning
171 based on the sample size:resolution trade off that limits CT studies [Wildenschild et al., 2002].
172 The porous ceramic was first submerged in de-aired deionized water and a vacuum applied to
173 ensure no air bubbles remain trapped within the ceramic. The plastic chamber had an O-ring
174 seal at the base and a flange, which was screwed together to ensure an air-tight fit. All
175 components of the chamber were made from plastic to avoid possible image artefacts, which
176 could result from using high X-ray attenuating construction materials such as metal. A 0387
177 Millipore vacuum pump (Merck Millipore, MA, USA) was attached to the chamber and the
178 soil columns were initially saturated from below with deionized water before being placed

Deleted:

Deleted: put

181 under a vacuum of -5 kPa (50.8 mmHg), -10 kPa (76.2 mmHg), -20 kPa (152.4 mmHg), -40
182 kPa (304.8 mmHg), -60 kPa (457.2 mmHg) and -75 kPa (533.4 mmHg). ~~It was not possible to~~
183 ~~achieve~~ pressures in excess of -75 kPa in the system described. The vacuum pump was ~~enabled~~
184 for 120 min then the valve sealed to retain the vacuum inside the chamber. At each matric
185 potential the soil core inside the chamber was scanned (further details in next section). After
186 each scan the soil core was removed from the chamber and weighed to calculate gravimetric
187 water content.

188

189 Using a combination of sand tables, pressure plates and pressure membrane apparatus, the
190 WRC were obtained for both soil types. Using conventional methods the van Genuchten model
191 [*van Genuchten*, 1980] was fitted to the data. The sand table was prepared by filling the water
192 reservoir and raising it above the base height of the table to ensure full saturation of the sand
193 table with no air bubbles. Both undisturbed field cores and sieved samples (packed to a bulk
194 density of 1.2 g cm⁻³) were placed flat on the sand table. To obtain the mid-range points on the
195 WRC, a pressure plate Model 1600 Pressure Plate Extractor (Soil Moisture Corp, Santa
196 Barbara, CA, U.S.A) was used. Samples were placed on the plate and the samples were
197 weighed frequently until equilibrating at a series of matric potentials. To obtain measurements
198 at lower matric potentials, a pressure membrane apparatus was used. For the sieved samples
199 the required mass of soil was carefully placed into the metal vessels of the pressure membrane
200 apparatus and saturated with air-free water. The field core samples were directly collected in
201 the metal cores and placed onto the apparatus. The collection tubes were weighed frequently
202 and once equilibrated the system was adjusted to higher pressures. After the final measurement,
203 soil samples were oven dried at 105 °C for 24 hr then weighed.

204

Deleted: Despite testing

Deleted: , further

Deleted: were not possible

Deleted: turned on

209 The measured volumetric water content of the field structured soil cores (θ), accounted for the
210 likely presence of stones and their overall influence on the WRC [Gardner, 1965; Reinhart,
211 1961]. The volumetric water content of the soil is written as θ which is measured in $\frac{\text{cm}^3(\text{H}_2\text{O})}{\text{cm}^3(\text{Soil})}$.
212 To calculate this a correction was applied to the measured volumetric water content of the
213 sample, θ_m , which is measured as $\frac{\text{cm}^3(\text{H}_2\text{O})}{\text{cm}^3(\text{Total})}$. This stone correction was calculated using

$$\theta = \theta_m \left(1 + \frac{V_s}{V_f} \right), \quad (1)$$

214 where V_f is the fine soil volume measured in $\text{cm}^3(\text{soil})$ and V_s is the volume of stones which
215 is measured in $\text{cm}^3(\text{stones})$ and calculated by subtracting the soil volume from the total
216 sample volume.

217

218 3.3. X-ray Computed Tomography and analysis

219 Four replicates from each soil type of the field cores were scanned at the seven matric potentials
220 giving a total of 56 scans for the field structured cores. As they would not be used for individual
221 pore characterisation analysis only three replicates were scanned for the sieved soils leading to
222 42 additional scans and a total overall number of 98 scans. The field of view for each scan
223 included the entire sample and each scanned sample created a dataset approximately 25
224 gigabytes in size, which includes all the associated image stacks for analysis, therefore 2.4
225 terabytes of data was collected. X-ray CT scanning was performed using a Phoenix Nanotom
226 180NF (GE Sensing & Inspection Technologies GmbH, Wunstorf, Germany). The scanner
227 consisted of a 180 kV nanofocus X-ray tube fitted with a diamond transmission target and a 5-
228 megapixel (2316 x 2316 pixels, 50 x 50 μm pixel size) flat panel detector (Hamamatsu
229 Photonics KK, Shizuoka, Japan). A maximum X-ray energy of 100 kV and 140 μA was used

Deleted: giving a total of

Deleted: so overall

232 to scan each soil core. A total of 1440 projection images were acquired over a 360° rotation.
233 Each projection was the average of 3 images acquired with a detector exposure time of 1 s.
234 The resulting isotropic voxel edge length was 10.17 μm and total scan time was 105 minutes
235 per core. Although much faster scan times are possible it was necessary in this instance to use
236 a longer scan time to acquire the highest quality images to aid with the phase separation. Two
237 small aluminium and copper reference objects ($< 1 \text{ mm}^2$) were attached to the side of the soil
238 core to assist with image calibration and alignment during image analysis. Reconstruction of
239 the projection images to produce 3D volumetric data sets was performed using the software
240 `datos|rec` (GE Sensing & Inspection Technologies GmbH, Wunstorf, Germany).

241

242 The reconstructed CT volumes were visualised and quantified using VG StudioMAX® 2.2
243 (Volume Graphics GmbH, Heidelberg, Germany). Air, soil and water phases of the scanned
244 volume were segmented separately using a threshold technique based on the greyscale value
245 of each voxel using a calibration tool within VG StudioMax v2.2. This works by selecting
246 specific areas of the scanned volume based on greyscale values, which are a result of (X-ray
247 attenuation) density differences within the sample. Image segmentation is the classification of
248 voxels within a CT volume that share common grayscale values and thus X-ray attenuation.
249 The calibration tool allows the user to sample the greyscale value of a selection of voxels that
250 correspond to the background (*e.g.* the phase/s not considered, this is usually the background
251 air) and then the process is repeated for voxels that correspond to the material of interest (*e.g.*
252 water, air or soil). Based on the greyscale range we segmented all voxels above a 50% mean
253 value between the background and material of interest and define them as a particular phase
254 (i.e. a region of interest). In a two phase sample air is usually used as the background greyscale
255 value to calibrate against. However, as we required the segmentation of three phases, two

Deleted: inside each chamber for each scan

257 vessels, one containing soil pore water and the other finely sieved soil ($< 100 \mu\text{m}$) for either
258 the sand or clay soil were securely fitted to the inside of the chamber for each scan. The soil
259 pore water and finely sieved soil remained separate from the soil core, but within the imaging
260 field of view, which was important as the soil core sample can change in overall greyscale
261 range over the course of the experiment due to localised drying and X-ray filament aging. Using
262 this approach these separate vessels were used as reference objects during image analysis. It
263 was important that reference vessels were included in every scan as CT scanning is subject to
264 minor variations in greyscales between scans as the system filament ages. A schematic
265 representation of the water segmentation method is presented in Supplementary Figure 2. The
266 first stage was to create a region of interest (ROI) that included all phases except the air filled
267 pore space. This was done by selecting the air space around the sample as the background,
268 ensuring all voxels except those of air would be included as the material of interest and a 3D
269 ROI was then created and labelled 'Water and soil ROI' *e.g.* air not included. The process was
270 then repeated, but utilising the soil inside the reference vessel as a reference value for the solid
271 material. It was used as a reference as it contained limited water and air, hence this 3D ROI
272 was labelled 'Soil'. Subtraction of the 'Soil ROI' from the 'Water and soil ROI' resulted in a
273 ROI with voxels of grey scale values attributed to 'soil water only', *e.g.* the range of voxels
274 remaining after the soil and air ROIs have been subtracted. The volume of the resulting 'Soil
275 Water' ROI was validated against the water reference object and traditional methods of
276 determining volumetric water content (weighing). Using this approach we assume all organic
277 matter is classified as 'soil'. To create an ROI that included solely the air filled pore space, the
278 ROI that included all material except the air was inverted using the 'Invert ROI' function in
279 VG_StudioMax software. The volume analyser tool in VG StudioMax was subsequently used
280 to quantify the total volume of the air and water filled pores. Reconstructed volumes for each
281 matric potential were aligned in VG_StudioMax using the metal reference objects on the outside

Deleted: throughout

Deleted: i

Deleted: a

Deleted: everything, but

Deleted: everything else

Deleted: was

Deleted: used

Deleted: that

Deleted: just

Deleted: everything but

Deleted:

Deleted: manually

Deleted:

295 of the sample container. After segmentation of the soil core volumes, a cylindrical ROI shape
296 template was used to subtract the surrounding column and air space from the volume to remove
297 the cylinder of soil. This template was used to ensure the same volume was used for each
298 sample before analysis. No significant evidence of shrinkage was observed across the range of
299 low matric potentials considered here. We note that when three phases (air water and soil) are
300 present in an image erroneous films of the intermediate phase can often be segmented out
301 between the high and low density phases. In this case erroneous films of water could be
302 introduced through segmentation. However, as thin water films only contribute a total flow
303 proportional to the third power of the film thickness these are not a concern in this study.

Deleted: cropped

305 Image stacks of the extracted volumes were exported and subsequently analysed for individual
306 water filled and air filled pore characteristics for the field structured soil only using ImageJ
307 v1.42 (<http://rsbweb.nih.gov/ij/>) [Ferreira and Rasband, 2011]. For 2D analysis objects less
308 than two pixels (twice the resolution) in diameter (0.02 mm) and for 3D analysis objects less
309 than two voxels in each direction ($8 \times 10^{-6} \text{ mm}^3$) were regarded as potential noise as a
310 precaution [Wildenschild *et al.*, 2005], and subsequently excluded from the analysis. The BoneJ
311 plugin algorithm [Doube *et al.*, 2010] (<http://bonej.org/>) in ImageJ software was used to
312 measure discrete individual 3D water filled and air filled pore characteristics namely volume,
313 surface area and thickness (diameter). A voxel is classed as connected to another voxel if it at
314 least touches corner to corner. ImageJ was used to measure the 2D pore shape characteristic
315 ‘circularity’, which is a measure of an object’s similarity to a circle. A value of 1 describes a
316 perfect circle and as the value decreases, the object becomes increasingly elongated. The
317 circularity was determined using

Deleted: 20 μm

Deleted: 80 μm^3

Deleted: and subsequently excluded from the analysis

Deleted: .

Deleted: -

Deleted: perfect

Deleted: would be

318
$$C = \frac{4\pi(A_p)}{(P_p)^2}, \quad (2)$$

327 where A_p is the pore area and P_p is the pore perimeter. The water-filled pore image stack was
328 skeletonised and from this the 3D connectivity (the sum of all the thin (1 voxel) pathways that
329 still preserve the connected topology and original shape of the object) of the water-filled pore
330 volume was also calculated.

331
332 In order for the geometries of the water-filled pores to be modelled, surface mesh files (.stl)
333 were required, which were generated in VG StudioMax v2.2. After segmentation of the soil
334 water phase, a cube shaped ROI template was imported to create identical cubes for the surface
335 mesh generation. Each sample was subsampled, from random initial coordinates, with 6 cubes
336 comprising side lengths of 3.8 mm. The same coordinates were used for different matric
337 potentials of the same sample. Each individual surface mesh file took between 0.5 – 2 hours to
338 generate depending on the complexity of the surface.

Moved (insertion) [1]

Deleted: ; these

340 3.4. Modelling

341 The hydraulic conductivity of the soil was calculated using the method of homogenization
342 [Pavliotis and Stuart, 2008]. This method allows an average Darcy's law to be defined which
343 is applicable to the soil column and is parameterised by the pore scale geometry of the soil.
344 The key assumption used was that the hydraulic properties of the soil can be accurately
345 captured by studying a small subsample of the soil [Fowler, 1997], this is often referred to as
346 the Representative Elementary Volume (REV). In this paper we were particularly interested in
347 determining the minimum size REV for which the calculated hydraulic conductivity converges
348 to the macroscopic hydraulic conductivity for soil samples of the order of a few millimetres.

Moved up [1]: In order for the geometries of the water-filled pores to be modelled, surface mesh files (.stl) were required; these were generated in VG StudioMax v2.2. After segmentation of the soil water phase, a cube shaped ROI template was imported to create identical cubes for the surface mesh generation. Each sample was subsampled, from random initial coordinates, with 6 cubes comprising side lengths of 3.8 mm. The same coordinates were used for different matric potentials of the same sample. Each individual surface mesh file took between 0.5 – 2 hours to generate depending on the complexity of the surface.

Deleted: ¶

361 This method allowed us to theoretically determine the required sample size for CT analysis of
362 water flow in soil at this scale.

Deleted: on

Deleted: ¶

363
364 We note that the averaged hydraulic conductivity and WRC calculated at this scale are not
365 globally applicable. Rather they describe the average flow rate in soil of this type assuming no
366 large scale features such as cracks or larger voids are encountered. In theory these features
367 could be included by deriving an averaged Darcy's law for each soil type. Stokes' equations
368 for large void spaces and approximate Darcy's laws for fractures equation [Hornung, 1997].
369 These systems could, in principle, be upscaled to derive averaged Darcy's laws on a much
370 larger scale. However, in this paper our focus is in obtaining an estimate of the hydraulic
371 properties of soils based on their pore structure. Hence, we neglect these larger scale features
372 but emphasise that they could be included through an additional level of upscaling.

Deleted: on

Deleted: that

Deleted: ,

Deleted: or regions of different porosity

Deleted: we are interested

373
374 As we are able to segment the air and water separately from the CT images, the fluid dynamics
375 can be greatly simplified. Rather than focusing on the moving interface between each phase,
376 we consider the relatively slow, flow of water about a fixed interface. The resulting equations
377 are introduced in the appendix. We further simplify the equations by assuming that the non-
378 wetting phase, in this case air, is stationary. This assumption is valid assuming that the air
379 phase is disconnected. If this is not the case then the movement of the air effectively lubricates
380 the movement of water resulting in an increase in the hydraulic conductivity. This approach is
381 valid assuming that the pressure gradients are sufficiently low, such that the interface remains
382 fixed, and that the non-wetting phase is not connected, hence, the trapped non-wetting phase
383 has zero average velocity.

Deleted: consider

392

393 Strictly speaking the theory of homogenization requires the soil structure to be periodic. Clearly
394 for real soil samples this is not the case. This is overcome by enforcing an apparent image
395 based periodicity either by translation or reflection of the CT image (Figure 1). In this paper
396 reflection was chosen as it simplifies the resulting calculations and does not introduce
397 discontinuities in the soil structure. The error induced by enforcing periodicity is that the
398 geometry considered numerically is now fully periodic rather than quazi-periodic and does not
399 truly represent the imaged soil structure. To overcome this, different size REV's were taken
400 from the segmented .stl files, see Figure 1. Specifically, the 6 cubes which were segmented
401 from each scan were of the same volume $V_m = 54.9 \text{ mm}^3$, and were assumed to be sufficiently
402 large that the soil properties would have converged. The REV's sampled from the six cubes
403 were of volume $V = V_m/(2^j)$, where j is a positive integer in the range 0 to 10 such that the
404 smallest volume we consider is 0.053 mm^3 and the largest is V_m . As j is decreased and, hence,
405 the size of the REV is increased, the relative size of the errors induced by the reflection
406 decreases. Similarly as the REV size increases, the hydraulic properties of the subsample will,
407 in principle, converge to the hydraulic properties of the soil.

408

409 A rigorous analysis of equations governing fluid flow through soil is given in [Daly and Roose,
410 2014]. Here we provide a brief description of the theory in the applied context with further
411 details given in the appendix. We consider a sample of soil which is large with respect to the
412 REV size. Specifically if the REV is a small cube with side length L_y and the large sample we
413 are interested in has characteristic length L_x then we require that the ratio of these two lengths
414 is small, *i.e.*, $\epsilon = L_y/L_x \ll 1$. For typical pore sizes observed in soil, the viscous forces
415 dominate [Fowler, 1997]. Hence, we may consider the Stokes limit of the Navier-Stokes

Deleted: n

Deleted: n

Deleted: 8

Deleted: 2

Deleted: n

421 equations where all inertial terms are neglected. Mathematically the macroscopic hydraulic
 422 conductivity, which is valid for the whole soil column, is obtained in two steps. First, it is
 423 shown, see appendix for details, that pressure variations across the REV of size ϵ will induce
 424 a water velocity also of size ϵ . Secondly, a set of equations are derived which allow the
 425 pressure driven fluid velocity to be determined based on the soil (Figure 1). Finally, the average
 426 velocity over the REV is used to determine a Darcy's law which is independent of ϵ . This value
 427 is valid for the bulk soil and describes fluid driven by an external pressure gradient, see [Daly
 428 and Roose, 2014]

Deleted: '

Deleted: unit cell

Deleted: only affect the average water

Deleted: by a quantity

$$\mathbf{u} = -\mathcal{K}(\nabla p_0 - \rho g \hat{\mathbf{e}}_z), \quad (3)$$

429 where ρ is the fluid density ($\rho = 10^3 \text{kg m}^{-3}$ in the case of water), $g = 9.8 \text{m s}^{-2}$ is the
 430 acceleration due to gravity, p_0 is the applied pressure, \mathbf{u} is the volume averaged water velocity
 431 and \mathcal{K} is the relative permeability (in the general case a tensor) which has components defined
 432 as

$$\mathcal{K}_{jk} = \frac{L_y^2}{\mu} \int_{\Omega_w} \hat{\mathbf{e}}_j \cdot \mathbf{v}_k^w dy. \quad (4)$$

433 Here $\hat{\mathbf{e}}_j$, for $j = x, y, z$ is a unit vector in the j -th direction and \mathbf{v}_k^w is the local velocity.
 434 Assuming that the air velocity is slower than the water velocity then \mathbf{v}_k^w satisfies the cell
 435 problem

$$\nabla \cdot \sigma_k^w - \nabla \pi_k^w = \hat{\mathbf{e}}_k, \quad \mathbf{x} \in \Omega_w, \quad (5a)$$

$$\nabla \cdot \mathbf{v}_k^w = 0, \quad \mathbf{x} \in \Omega_w, \quad (5b)$$

$$\mathbf{v}_k^w = 0, \quad \mathbf{x} \in \Gamma_s, \quad (5c)$$

$$\mathbf{v}_k^w = 0, \quad \mathbf{x} \in \Gamma_{aw}, \quad (5d)$$

440 where $\sigma_k^w = (\nabla \mathbf{v}_k^w) + (\nabla \mathbf{v}_k^w)^T$, π_k^w is the local pressure correction due to the microscale
441 geometry, the superscript w denotes the water phase, Ω_w , Γ_s and Γ_{aw} denote the water domain,
442 the soil boundary and the air-water interface respectively. Physically this can be thought of as
443 calculating the fluid velocity subject to a unit pressure gradient. As the equations are linear
444 Darcy's law follows by multiplying the result by the desired pressure gradient.

445

446 Equations (5) were solved numerically on each subsample obtained from the CT images using
447 OpenFOAM, an open source Computational Fluid Dynamics toolbox running on IRIDIS, the
448 High Performance Computing Facility at the University of Southampton. The hydraulic
449 conductivity is then calculated as the average water velocity due to gravity. Results were
450 obtained for each soil sample using the method illustrated in Figure 1. The 6 cube surface
451 meshes, generated from each soil core, were repeatedly sampled to obtain 3D REV's of
452 increasing size. The result is a set of hydraulic conductivity calculations which we expect to
453 converge to the true hydraulic conductivity of the soil, at each point along the WRC, as the
454 sub-volume size is increased.

455

456 3.5. Statistical analysis

457 The results obtained directly from the CT images were analysed by general analysis of
458 variance (ANOVA) containing soil type and matric potential and all possible interactions
459 as explanatory variables using Genstat 15.1 (VSN International, UK).

460

461 4. Results & Discussion

462

463 4.1 Hydraulic properties

464

465 The clay soil contained an average stone volume of 0.2 cm³ whereas the average stone volume
466 for the sand soil was 5.5 cm³ (total soil volume was 55 cm³). Therefore although field structured
467 soil was able to retain water for longer, as shown by the curves from the conventional method
468 (Figure 2), the influence of stones was not a consideration and the greater water holding
469 capacity is attributed to the more complex pore network in the field structured soil.

Deleted: samples

Deleted: samples

Deleted: is

470

471 There are clear differences between sieved soil and field structured soil (Figures 2 and 3). For
472 the field structured soil the imaging technique shows a good agreement with the conventional
473 methods with an average error of $\leq 5\%$ across the range of matric potentials considered. The
474 sieved soil responded more strongly to pressure change in comparison to the field structured
475 soil. However, the imaged sieved soil data did not show this trend, hence, there was quite a
476 large error of 9% at 0 kPa and as high as 65% at -75 kPa. This suggests that, for the field
477 structured samples, the segmentation procedure was successful at identifying the majority of
478 the water filled pores (WFPs).

Deleted: less than

479

480 It is somewhat surprising that the more homogeneous sieved soil is less well represented
481 through the imaging technique than the field structured soil. However, we attribute this to the
482 pore size distribution in the two soils. The field structured soil has a wider range of pore sizes
483 than the sieved soil which contains macropores defined by the largest grain size. As the matric
484 potential becomes increasingly negative, the water drains from smaller and smaller pores. In

Deleted: this can be

Deleted: d

Deleted: is likely

Deleted: have

Deleted: will

Deleted: is made

495 the case of the field structured soil this results in a gradual decrease in volumetric water content
496 with matric potential which the imaging technique can follow assuming the pore size is larger
497 than the image resolution. In the case of the sieved soil there is a reduced range of pore sizes
498 and the water quickly drains from the larger pores and remains trapped in a large number of
499 smaller pores. The result is that the volumetric water content drops quickly as the matric
500 potential is reduced and the imaging technique, which cannot resolve the smallest pores, fails
501 to capture this. We also note that the differences observed in the WRC between the two soil
502 types is smaller when measured using the imaging technique than using conventional methods.
503 This is again attributed to the finite resolution of the measurements and is analogous to the
504 increasing error observed as the saturation is decreased.

505

506

507 The hydraulic conductivity, which corresponds to the water release curves shown in Figure 2,
508 has been calculated by solving equations (5) for increasing subsample size. As the subsample
509 size was increased, the hydraulic conductivity converged to a fixed value which we interpret
510 as the macroscopic hydraulic conductivity (Figure 4). The sample size at which this occurred
511 was smaller for lower matric potentials. This is attributed to the increased air-filled porosity
512 which decreases the contact area between the water and the soil. Hence, the effect of the
513 heterogeneous soil boundary is decreased and the overall homogeneity of the sample is
514 increased. We note that, as convergence is seen to occur at smaller sample sizes for lower
515 saturation, fewer simulations were run at these saturation values. This occurs at approximately
516 $\frac{1}{4}$ of the sample volume for all matric potentials for both soils. We note that although the REV
517 volume is approximately the same for all soil types considered, the properties obtained from
518 this analysis are different for different soil types. This method therefore enabled the required

Deleted: the macroscopic

Deleted: values

521 sample size for CT analysis of water flow in these samples to be determined, which was a cube
522 volume of 11 mm³. This sample was large enough for convergence of the calculated hydraulic
523 conductivity, meaning that the sample size contained an adequate volume of soil to capture the
524 averaged hydraulic properties on this scale. ~~Therefore considering~~ the averaging method used
525 in this paper, the hydraulic conductivity is globally valid. This means that the representative
526 volume of 11 mm³ is an appropriate representative volume element for the global hydraulic
527 conductivity of the soil samples used in this study. However, there may be significant features,
528 such as cracks or heterogeneities in the soil, which are not captured in the 11 mm³ volume.
529 Hence, ~~care~~ must be taken in applying these results on the field scale and an additional level of
530 upscaling may be required to capture the properties of these features.

Deleted: soil

Deleted: We note that, due

Deleted: to

Deleted: se

Deleted: s

Deleted: some

Deleted: .

531
532 The method described in Section 3.4 and the appendix allowed us to also obtain the hydraulic
533 conductivity in unsaturated soils as well as in x , y and z directions. It was expected the flow
534 would be dominant in the z direction due to gravity, however (possibly due to the size of the
535 samples) we did not observe this. The calculated hydraulic conductivities are shown as a
536 function of matric potential in Figure 5. The calculated hydraulic conductivities and the
537 corresponding WRC have been fitted to the van Genuchten model for the WRC and the
538 unsaturated hydraulic conductivity [*van Genuchten*, 1980] using a non-linear least squares
539 method. We note that we have only done this fitting for the imaged data as we do not have
540 hydraulic conductivity measurements for the full range of matrix potentials using conventional
541 measurements. The volumetric water content θ is given by

Deleted: that

$$\theta = (\theta_s - \theta_r) \left(\frac{1}{1 + (\alpha h)^n} \right)^m + \theta_r, \quad (6)$$

550 where θ_s and θ_r are the saturated and residual volumetric water content respectively, h is the
 551 is the matric head, $m = 1 - 1/n$ and n and α are the van Genuchten parameters. The
 552 corresponding hydraulic conductivity is given by $K = K_{sat}k_r^{vg}$. Here K_{sat} is the saturated
 553 hydraulic conductivity and the relative hydraulic conductivity is given by

$$k_r^{vg} = \frac{\{1 - (\alpha h)^{n-1}[1 + (\alpha h)^n]^{-m}\}^2}{[1 + (\alpha h)^n]^{m/2}} \quad (7)$$

554 We take θ_r to be negligible and fit the remaining parameters to the imaged data. The average
 555 saturated hydraulic conductivity and the fitted parameters: K_{sat} , θ_s , α and n are shown in Table
 556 1. The fitted hydraulic conductivity and WRC, obtained using these parameters, are shown in
 557 Figure 5.

558 **Table 1. Fitted van Genuchten parameters**

Soil	Measured K_{sat} [$cm s^{-1}$]	Calculated K_{sat} [$cm s^{-1}$]	Saturated volumetric water content θ_s	α [cm^{-1}]	n
Sand	0.0013	0.0014	0.418	0.153	1.71
Clay	0.0004	0.0010	0.423	0.148	1.66

559
 560 The hydraulic conductivity decreases as the matric potential decreases from 0 kPa to -75kPa
 561 ($P < 0.001$) and is slightly larger in the sand soil compared to the clay soil. The van Genuchten
 562 model fits the imaged data well with a slight discrepancy in the WRC at 0 kPa (RMSE=0.016
 563 for the clay soil and RMSE=0.022 for the clay soil). The experimentally measured hydraulic
 564 conductivity agreed well with the calculated value for the sand soil. However, the data
 565 compares less favourably in the case of the clay soil where the experimentally measured
 566 hydraulic conductivity is less than half that of the calculated value.

567

Deleted: hydraulic

Deleted: t

570 The differences observed for the clay soil between the experimentally measured hydraulic
571 conductivity and the calculated values are attributed to a combination of image resolution and
572 segmentation limitations. Typically clay soils have much smaller pores than sand soils, due to
573 the differences in particle size and as such will have a large number of pores which are
574 comparable with or below the imaging resolution used in this study. Further complications
575 include partial volume effects, which can cause errors in voxel classification, if the boundary
576 is between two phases with wide ranging attenuation values, such as air and rock [*Ketcham
577 and Carlson, 2001*]. This therefore could lead to an incorrect classification of voxels resulting
578 in either an overestimate or an underestimate of the pore space and pore size distribution due
579 to the effect it has on objects of differing sizes, which may explain why we have an
580 overestimation at the wet end, and underestimation at the dry end. As the calculated hydraulic
581 conductivity is large with respect to the measured value we expect that the pore space is being
582 over estimated in this case.

583

584 *4.2 Pore characteristics*

585 In order to obtain a better understanding of the pore scale processes which contribute to the
586 macroscopic hydraulic properties we consider the distribution of air and water within the soil
587 matrix on the pore scale. In order to quantify the air and water content we define Air Filled
588 Pores (AFPs) and Water Filled Pores (WFPs) as single connected regions of air or water
589 respectively. We also define the pore space as the union of all the AFPs and WFPs. Throughout
590 this paper when discussing connected regions of water and air we exclusively use this
591 terminology in keeping with the soil science literature. In addition we refer to individual pores
592 within the soil to define simply connected pathways between two distinct points within the
593 pore space. Typically, the pore space contains a single large WFP which contains over 50% of

Deleted: , this

Deleted: and

596 the water within the pore space and a large number of much smaller AFPs and WFPs. The
597 connected WFPs are the main contributor to both the WRC and the hydraulic conductivity
598 calculations. However, insight may be gained into the wetting and drying behaviour of the
599 soils by considering the properties of the AFPs. It is possible to determine the interfacial area
600 between water and air phases [Costanza-Robinson et al., 2008]. However, as previous studies
601 have made the calculations based on porous media other than soil, this is not comparable to the
602 work undertaken in this study. In addition the majority of ~~the previous work in soil~~ [Falconer
603 et al., 2012; García-Marco et al., 2014; Tucker, 2014], refer directly to WFPs and AFPs as
604 such it is more meaningful in the context of the literature to consider the WFP and AFP surface
605 area.

Formatted: Font color: Text 1

Formatted: Font color: Text 1

Deleted: researchers working in soil science

Formatted: Font color: Text 1

606
607 At 0 kPa we have a residual AFP volume of approximately 6% of the total pore space, see
608 supplementary Figure 3. This volume corresponds to trapped air pockets which, due to the high
609 tortuosity of the soil structure, remain in the pore space at saturation. As the matric potential
610 is made more negative, the total WFP volume decreases and the corresponding AFP volume
611 increases (Figure 6; $P < 0.001$). In addition to the change in WFP and AFP volume, the total soil
612 volume is seen to increase by up to 10%. Whilst this may, in part, be attributed to segmentation
613 issues and partial volume effects, it is also likely that changes in soil structure are responsible
614 for this apparent increase. The total AFP volume and the corresponding AFP surface area did
615 not vary significantly across the different soil types (sand and clay). However, the average
616 volume and the corresponding surface area of an individual AFP averaged across all matric
617 potentials shows significant variation across soil types ($P < 0.001$) with average AFP volume of
618 0.00115 mm^3 in the clay soil compared with 0.00163 mm^3 in the sand soil and with average
619 AFP surface area of 0.0109 mm^2 in the clay soil and 0.0182 mm^2 in the sand soil. This greater
620 surface area corresponds to a much greater number of AFPs at -75 kPa in the clay soil (104

622 pores/mm³) than the sand soil (55 pores/mm³), (P<0.05). The average pore thickness
623 decreased significantly with decreasing matric potential (Figure 7; P<0.001), from an average
624 of 0.030 mm at 0 kPa to 0.026 mm at -75 kPa. There was no significant difference between soil
625 types. At 0 kPa the average pore thickness for the clay soil was 0.027 mm compared to 0.033
626 mm for sand. At -75 kPa the average pore thickness for the clay and the sand soils was just
627 0.026 mm.

628
629 To highlight the differences in the soil types we classify the AFPs as air filled macro (> 100
630 μm), air filled meso (30 - 100 μm) and air filled micropores (21 – 30 μm), see supplementary
631 Figure 4. This classification is based on the pore diameter, *i.e.* the maximum sphere diameter
632 which can fit inside the pore. The air filled micropore range is limited by the achievable
633 resolution based on our estimation of image noise (> 2 voxels). As the matric potential is
634 decreased, the total number of AFPs classified into each category changes with an overall
635 increase in the number of air filled macropores seen in the case of the sand soil. In the sand
636 soil there is a linear increase in the percentage of air filled macropores with soil drainage, this
637 was expected due to the high number of macropores throughout the sand structure, which is
638 typically more homogenous compared to the clay. The clay soil had a less regular drainage
639 pattern than the sand soil. There is a linear increase in the air filled micropore percentage as
640 the clay dried. However, the percentage of air filled macropores is quite irregular and can be
641 attributed to the occurrence of crack formation which is more likely in clay soil. The average
642 pore circularity of the AFPs, equation (2), also increased as matric potential decreased. At -75
643 kPa the AFP space was comprised of pores with an average circularity of 0.78 compared to a
644 circularity value of 0.72 at 0 kPa (P<0.001). Our results also show that at drier matric potentials
645 the shape of the air and water filled pores become increasingly rounded possibly linked to air
646 bubble-style pore formation. This measurement enables us to quantify the influence of pore

Deleted: per

Deleted: per

Deleted: It is possible to determine the interfacial area between water and air phases [Costanza-Robinson *et al.*, 2008], however as previous studies have made the calculations based on glass beads and pure sand mixtures, this is not comparable to the work undertaken in this study. However, further investigation into this measurement for porous media with two fluid flows would be of interest. Our work agrees with Kibbey [2013], in that microscopic surface roughness is likely to have a relatively small effect on the accuracy of the fluid flow at the air and water boundaries providing that the surface scale of the surface roughness is sufficiently small [Daly and Roose, 2014]. This means our imaging resolution should not be a limiting consideration on the surfaces obtained [Brusseau *et al.*, 2010]. ¶

Deleted: determined

Deleted: .

Deleted: t

Deleted: gives

Deleted: a

Deleted: ication

Deleted: of

Deleted: drainage on

669 shape on soil drainage. However we note this is only a single measure and further descriptors
670 that account for the shape of the soil porous architecture in 3D are required to advance
671 understanding in this area. The 3D connectivity of the WFPs decreased with decreasing matric
672 potential ($P < 0.05$), pore connectivity was significantly greater in the clay soil at all matric
673 potentials ($P < 0.01$). The differences in the AFP structure in the two soil types are indicative
674 of the soil structure. The clay soil contains a large number of micro-pores which corresponds
675 to the large number of air filled micropores trapped within the soil structure. In contrast the
676 sand soil contains a larger number of meso- and macro-pores causing the air to be contained in
677 relatively few, larger volumes. It is highly likely that the clay soil contained many pores that
678 were too small to be imaged at the achievable resolution in this study.

Deleted: ,

Deleted: h

Deleted: are urgently required for this type of work

Deleted: .

Deleted: more

680 5. Conclusions

681

682 In this paper we have used a combination of CT imaging and mathematical modelling to derive
683 the WRC and unsaturated hydraulic conductivity in contrasting soil textures (*i.e.* clay and sand)
684 and structures (*i.e.* sieved and field structured soil). The ability to non-destructively scan the
685 soil cores and segment the water and air filled pores from the soil matrix combined with the
686 mathematical modelling have provided a unique insight into the WRC and hydraulic properties
687 of contrasting soils. A comprehensive study of the hydraulic properties of different soil types
688 based on a quantitative visual assessment of the soil structure has been carried out across a
689 range of different saturation values. The results predict the increase in hydraulic conductivity
690 with saturation and highlight the structural basis for the differences between sand and clay
691 soils.

Deleted: the

692

699 The data obtained via CT imaging allows us to visualise the soil structure in 3D and, hence, to
700 measure the effects of pore geometry on the WRC. Using the scanned geometry combined with
701 detailed mathematical modelling, the unsaturated hydraulic conductivity and, hence, hydraulic
702 conductivities were obtained at the precise measured matric potentials. These values are not
703 easily measured in the laboratory through experimentation alone. Using the measured saturated
704 hydraulic conductivity and typical soil parameters we have compared the computed values
705 against the van Genuchten model. The simulated values compared well with the measured
706 saturated hydraulic conductivity values. The calculated hydraulic properties of the clay soil
707 against the van Genuchten model compare well. However, in the case of the sand soil, the
708 calculated values are lower than those obtained using the van Genuchten model. This
709 highlights the potential structural differences between two soils of a particular textural class
710 and the potential role played by the micro-porous structure of the aggregates which are
711 currently below the imaging resolution of CT for this sample size.

Deleted: structural

712
713 The combination of CT imaging and modelling provides a new level of understanding of the
714 role that structure plays in the averaged properties of soil. The WRC has been obtained via CT
715 imaging and provides a detailed geometric representation of how the water is retained in pores
716 of, different sizes. A downside to the imaging approach is the time investment required to
717 collect the data. However, this is comparable to the conventional laboratory method as the
718 majority of time is spent allowing the sample to equilibrate. However, this detailed information
719 on the pore-scale architecture represents a significant development in our ability to study soil
720 systems which will continue to advance pore scale modelling by providing three dimensional
721 geometries against which the numerical models can be tested [19].

Deleted: used in this paper

Deleted: the

Deleted: d pore

Deleted: The

722

728 **6. Acknowledgements**

729

730 The authors acknowledge the use of the IRIDIS High Performance Computing Facility, and
731 associated support services at the University of Southampton, in the completion of this work.

732 This project was funded by BBSRC BB/J000868/1, a collaborative project between
733 Southampton and Nottingham, PI and overall lead Roose. All reconstructed scan data will be
734 available on request by emailing microct@nottingham.ac.uk. The authors extend their thanks
735 to the anonymous reviewers for constructive feedback on their manuscript.

736

737 **Table A1. Values of parameters used in numerical calculations**

Constant	Value	Units	Description
ρ^w	10^3	kg m^{-3}	Density of water
ρ^a	1.2	kg m^{-3}	Density of air
μ^w	10^{-3}	$\text{kg m}^{-1} \text{s}^{-1}$	Viscosity of water
μ^a	20×10^{-6}	$\text{kg m}^{-1} \text{s}^{-1}$	Viscosity of air
\tilde{g}	9.8	m s^{-2}	Acceleration due to gravity
r_y	100×10^{-6}	m	Typical pore radius
L_y	10^{-3}	m	Typical size of microscale geometry
L_x	10^{-1}	m	Typical size of macroscale geometry
$\tilde{\gamma}$	7.28×10^{-2}	kg s^{-2}	Surface tension
$\tilde{\kappa}$	10^4	m^{-1}	Curvature
ϵ	10^{-2}		Ratio of geometry sizes
κ	2.97×10^2		Scaled surface tension-curvature product
$ \mathbf{g} $	1		Scaled gravitational force
δ_u	0.16		Typical velocity ratio
δ_p	8.33		Typical pressure ratio

738

739 **Appendix**

740 The starting point is the non-dimensional Stokes equations using the scaling given in [Daly and
741 Roose, 2014]. The dimensional variables, denoted with a $\tilde{\cdot}$, are scaled using

$$\begin{aligned} \mathbf{v}^w &= \frac{4\mu^w}{\rho^w \tilde{g} r_y^2} \tilde{\mathbf{v}}^w, & p^w &= \left(\frac{L_x}{L_y}\right) \frac{4L_y}{\rho^w \tilde{g} r_y^2} \tilde{p}^w, \\ \mathbf{v}^a &= \left(\frac{L_x}{L_y}\right) \frac{4\mu^a}{\rho^a \tilde{g} r_y^2} \tilde{\mathbf{v}}^a, & p^a &= \left(\frac{L_x}{L_y}\right)^2 \frac{4L_y}{\rho^a \tilde{g} r_y^2} \tilde{p}^a, \\ t &= \left(\frac{L_x}{L_y}\right) \frac{\rho^w r_y^2 \tilde{g}}{4\mu^w L_y} \tilde{t}, \end{aligned}$$

742 where \mathbf{v}^w and \mathbf{v}^a are the water and air velocities, p^w and p^a are the water and air pressures, t
743 is the dimensionless time and the remaining parameters are listed in table A1 and the non-
744 dimensional constants are

$\kappa = \left(\frac{L_y}{L_x}\right) \frac{4L_y \tilde{\gamma}}{\rho^w r_y^2 \tilde{g}} \tilde{\kappa},$	$\mathbf{g} = \frac{\hat{\mathbf{e}}_x L_y^3}{r_y^2 L_x},$	$\delta_u = \left(\frac{L_y}{L_x}\right) \frac{\rho^w \mu^a}{\rho^a \mu^w},$	$\delta_p = \left(\frac{L_y}{L_x}\right) \frac{\rho^w}{\rho^a},$
--	--	--	--

745 Typical values for the non-dimensional numbers are given in table A1. The resulting non-
746 dimensional Stokes equations are:

$$\epsilon \nabla \cdot \boldsymbol{\sigma}^w - \nabla p^w = \epsilon \mathbf{g} \quad \mathbf{x} \in \Omega_w, \quad (\text{A1a})$$

$$\epsilon \nabla \cdot \boldsymbol{\sigma}^a - \nabla p^a = \epsilon^2 \mathbf{g} \quad \mathbf{x} \in \Omega_a, \quad (\text{A1b})$$

$$\epsilon \phi \frac{\partial S^w}{\partial t} + \nabla \cdot \mathbf{v}^w = 0, \quad \mathbf{x} \in \Omega_w, \quad (\text{A1c})$$

$$\epsilon\phi \frac{\partial S^a}{\partial t} + \delta_u \nabla \cdot \mathbf{v}^a = 0, \quad \mathbf{x} \in \Omega_a, \quad (\text{A1d})$$

$$\mathbf{v}^w = 0, \quad \mathbf{v}^a = 0, \quad \mathbf{x} \in \Gamma_s, \quad (\text{A1e})$$

$$\hat{\mathbf{n}} \cdot \mathbf{v}^w = 0, \quad \hat{\mathbf{n}} \cdot \mathbf{v}^a = 0, \quad \mathbf{x} \in \Gamma_{aw}, \quad (\text{A1f})$$

$$\hat{\mathbf{t}} \cdot [\mathbf{v}^w - \delta_u \mathbf{v}^a] = 0, \quad \mathbf{x} \in \Gamma_{aw}, \quad (\text{A1g})$$

$$\hat{\mathbf{n}} \cdot [(\epsilon\sigma^w - Ip^w) - \delta_p(\epsilon\sigma^a - Ip^a)] = \hat{\mathbf{n}}\kappa, \quad \mathbf{x} \in \Gamma_{aw}, \quad (\text{A1h})$$

747 combined with periodic boundary conditions in the x y and z directions. To simplify the
 748 problem we notice that $\delta_u^{-1} < 1$ and $\delta_p < 1$ and, therefore, they can be neglected to first
 749 approximation. The result is that the air and water velocities decouple we need only consider
 750 the flow of water through the soil. The air velocity could in principle be calculated as a
 751 perturbation of order δ_u which in turn would create a water velocity perturbation of order
 752 δ_u/δ_p . However, we expect that this perturbation will be small with respect to the uncertainty
 753 in the segmentation and the temperature dependent variations of the water viscosity. The
 754 simplified equations are:

$$\epsilon \nabla^2 \mathbf{v}^w - \nabla p^w = \epsilon \mathbf{g} \quad \mathbf{x} \in \Omega_w, \quad (\text{A2a})$$

$$\nabla \cdot \mathbf{v}^w = 0, \quad \mathbf{x} \in \Omega_w, \quad (\text{A2e})$$

$$\mathbf{v}^w = 0, \quad \mathbf{x} \in \Gamma_s, \quad (\text{A2f})$$

$$\mathbf{v}^w = 0, \quad \mathbf{x} \in \Gamma_{aw}, \quad (\text{A2g})$$

755 We expand the gradient operator $\nabla = \epsilon \nabla_x + \nabla_y$ and look for a power series solution to
 756 equations (A4) of the form

$$\mathbf{v}^w = \mathbf{v}_0^w + \epsilon \mathbf{v}_1^w + O(\epsilon^2) \quad (\text{A3a})$$

$$p^w = p_0^w + \epsilon p_1^w + O(\epsilon^2) \quad (\text{A3b})$$

757 Substituting equations (A3) into equations (A2) and retaining terms $O(\epsilon^0)$ we obtain $\nabla_y p_0^w =$
 758 0 , *i.e.*, the largest component of the pressure is constant over the microscale. Expanding to
 759 $O(\epsilon^1)$ we effectively convert the leading order pressure drop into a body force and obtain

$$760 \quad \mathbf{v}_0^w = \sum_{k=1}^3 \mathbf{v}_k \partial_{x_k} p_0^w$$

761 Where \mathbf{v}_k satisfy the cell problem

$$\nabla_y^2 \mathbf{v}_k - \nabla_y \pi_k^w = \hat{\mathbf{e}}_k, \quad \mathbf{x} \in \Omega_w, \quad (\text{A4a})$$

$$\nabla_y \cdot \mathbf{v}_k = 0, \quad \mathbf{x} \in \Omega_w, \quad (\text{A4b})$$

$$\mathbf{v}_k = 0, \quad \mathbf{x} \in \Gamma_s, \quad (\text{A4c})$$

$$\mathbf{v}_k = 0, \quad \mathbf{x} \in \Gamma_{aw}, \quad (\text{A4d})$$

$$\mathbf{v}_k, \pi_k^w \text{ periodic with period } 1 \quad (\text{A4e})$$

762 Averaging the velocity over the unit cell we obtain the non-dimensional form of Darcy's law
763 for the average velocity

$$764 \quad \mathbf{u}_0^w = \int_{\Omega} \mathbf{v}_k \otimes \hat{\mathbf{e}}_k \, dy (\nabla_x p_0^w + \mathbf{g})$$

765 which in dimensional form is equation (3) and (4) in the main paper.

766 As discussed in the main text we impose periodicity via reflection of the geometry about the x,
767 y and z axis. The result is that the velocity is, for the k -th cell problem, the pressure correction
768 π_k^w is even odd in the direction x_k and even in the direction x_j for $j \neq k$. Similarly we find
769 that the k -th component of the velocity, $\hat{\mathbf{e}}_k \cdot \mathbf{v}_k$ is even in all directions. The remaining velocity
770 components, $\hat{\mathbf{e}}_j \cdot \mathbf{v}_k$ for $j \neq k$, are odd in the directions x_k and x_j , however, they are even in
771 the direction x_p for $p \neq k$ and $p \neq j$. Specifically the resulting boundary equations and
772 boundary conditions are:

$$\nabla_y^2 \mathbf{v}_k - \nabla_y \pi_k^w = \hat{\mathbf{e}}_k, \quad \mathbf{x} \in \Omega_w, \quad (\text{A5a})$$

$$\nabla_y \cdot \mathbf{v}_k = 0, \quad \mathbf{x} \in \Omega_w, \quad (\text{A5b})$$

$$\mathbf{v}_k = 0, \quad \mathbf{x} \in \Gamma_s, \quad (\text{A5c})$$

$$\mathbf{v}_k = 0, \quad \mathbf{x} \in \Gamma_{aw}, \quad (\text{A5d})$$

$$\pi_k^w = 0, \quad \frac{\partial}{\partial x_k} (\hat{\mathbf{e}}_k \cdot \mathbf{v}_k) = 0, \quad \hat{\mathbf{e}}_j \cdot \mathbf{v}_k = 0, \quad j \neq k \quad \mathbf{x} \in \partial x_k \quad (\text{A5e})$$

$$\frac{\partial}{\partial x_j} \pi_k^w = 0, \quad \frac{\partial}{\partial x_p} (\hat{\mathbf{e}}_p \cdot \mathbf{v}_k) = 0, \quad \hat{\mathbf{e}}_j \cdot \mathbf{v}_k = 0, \quad p \neq k, \quad p \neq j \quad \mathbf{x} \in \partial x_j \quad (\text{A5f})$$

773 where ∂x_k is the boundary located at $x_k = 0$ and $x_k = 1/2$, ∂x_j is the union of the boundaries
774 located at $x_j = 0$ and $x_j = 1/2$ for $j \neq k$.

775

776

777

778 7. References

779

780 Aravena, J., M. Berli, S. Ruiz, F. Suarez, T. Ghezzehei, and S. Tyler (2014), Quantifying
781 coupled deformation and water flow in the rhizosphere using X-ray microtomography and
782 numerical simulations, *Plant and Soil*, 376(1-2), 95-110.

783 Aravena, J. E., M. Berli, T. A. Ghezzehei, and S. W. Tyler (2011), Effects of Root-Induced
784 Compaction on Rhizosphere Hydraulic Properties - X-ray Microtomography Imaging and
785 Numerical Simulations, *Environmental Science & Technology*, 45(2), 425-431.

786 Arbogast, T., and H. L. Lehr (2006), Homogenization of a Darcy–Stokes system modeling
787 vuggy porous media, *Computational Geosciences*, 10(3), 291-302.

788 Blunt, M. J. (2001), Flow in porous media—pore-network models and multiphase flow,
789 *Current opinion in colloid & interface science*, 6(3), 197-207.

790 Blunt, M. J., B. Bijeljic, H. Dong, O. Gharbi, S. Iglauer, P. Mostaghimi, A. Paluszny, and C.
791 Pentland (2013), Pore-scale imaging and modelling, *Advances in Water Resources*, 51, 197-
792 216.

793 Bryant, S., and M. Blunt (1992), Prediction of relative permeability in simple porous media,
794 *Physical Review A*, 46(4), 2004.

795 Bryant, S., D. Mellor, and C. Cade (1993a), Physically representative network models of
796 transport in porous media, *AIChE Journal*, 39(3), 387-396.

797 Bryant, S., P. King, and D. Mellor (1993b), Network model evaluation of permeability and
798 spatial correlation in a real random sphere packing, *Transport in Porous Media*, 11(1), 53-70.

799 Clausnitzer, V., and J. W. Hopmans (2000), Pore-scale measurements of solute breakthrough
800 using microfocus X-ray computed tomography, *Water Resources Research*, 36(8), 2067-2079.

801 Costanza-Robinson, M. S., K. H. Harrold, and R. M. Lieb-Lappen (2008), X-ray
802 microtomography determination of air– water interfacial area– water saturation relationships
803 in sandy porous media, *Environmental science & technology*, 42(8), 2949-2956.

804 Crestana, S., S. Mascarenhas, and R. S. Pozzi-Mucelli (1985), Static and dynamic 3
805 dimensional studies of water in soil using computed tomographic scanning, *Soil Science*, 140,
806 326-332.

807 Daly, K. R., and T. Roose (2014), Multiscale modelling of hydraulic conductivity in vuggy
808 porous media, *Proceedings of the Royal Society A: Mathematical, Physical and Engineering*
809 *Science*, 470(2162).

810 Doube, M., M. M. Kłosowski, I. Arganda-Carreras, F. P. Cordelières, R. P. Dougherty, J. S.
811 Jackson, B. Schmid, J. R. Hutchinson, and S. J. Shefelbine (2010), BoneJ: Free and extensible
812 bone image analysis in ImageJ, *Bone*, 47(6), 1076-1079.

813 Falconer, R. E., A. N. Houston, W. Otten, and P. C. Baveye (2012), Emergent Behavior of Soil
814 Fungal Dynamics: Influence of Soil Architecture and Water Distribution, *Soil Science*, 177(2),
815 111-119 110.1097/SS.1090b1013e318241133a.

816 Fatt, I. (1956), The network model of porous media.

817 Ferreira, T. A. W. R., and W. Rasband (2011), The ImageJ User Guide, Version 1.45.,
818 (<http://rsbweb.nih.gov/ij/docs/user-guide.pdf>).

819 Fowler, A. C. (1997), *Mathematical models in the applied sciences*, Cambridge University
820 Press, U.K.

821 Gao, W., T. Ren, A. G. Bengough, L. Auneau, C. W. Watts, and W. R. Whalley (2012),
822 Predicting Penetrometer Resistance from the Compression Characteristic of Soil, *Soil Science*
823 *Society of America Journal*, 76(2), 361-369.

824 García-Marco, S., S. R. Ravella, D. Chadwick, A. Vallejo, A. S. Gregory, and L. M. Cárdenas
825 (2014), Ranking factors affecting emissions of GHG from incubated agricultural soils,
826 *European Journal of Soil Science*, 65(4), 573-583.

827 Gardner, W. H. (1965), Water Content, in *Methods of Soil Analysis. Part 1. Physical and*
828 *Mineralogical Properties, Including Statistics of Measurement and Sampling*, edited by C. A.
829 Black, pp. 82-127, American Society of Agronomy, Soil Science Society of America.

830 Haugen, Å., N. Mani, S. Svenningsen, B. Brattekkås, A. Graue, G. Ersland, and M. Fernø
831 (2014), Miscible and Immiscible Foam Injection for Mobility Control and EOR in Fractured
832 Oil-Wet Carbonate Rocks, *Transport in Porous Media*, 104(1), 109-131.

833 Helliwell, J. R., A. J. Miller, W. R. Whalley, S. J. Mooney, and C. J. Sturrock (2014),
834 Quantifying the impact of microbes on soil structural development and behaviour in wet soils,
835 *Soil Biology and Biochemistry*, 74(0), 138-147.

836 Hornung, U. (1997), *Homogenization and porous media*, Springer, Berlin, Germany.

837 Houston, A. N., W. Otten, P. C. Baveye, and S. Hapca (2013), Adaptive-window indicator
838 kriging: A thresholding method for computed tomography images of porous media, *Computers
839 & Geosciences*, 54(0), 239-248.

840 Iassonov, P., T. Gebrenegus, and M. Tuller (2009), Segmentation of X-ray computed
841 tomography images of porous materials: A crucial step for characterization and quantitative
842 analysis of pore structures, *Water Resources Research*, 45(9), W09415.

843 Keller, J. B. (1980), Darcy's law for flow in porous media and the two-space method, paper
844 presented at Nonlinear partial differential equations in engineering and applied science (Proc.
845 Conf., Univ. Rhode Island, Kingston, RI, 1979), Dekker New York.

846 Ketcham, R. A., and W. D. Carlson (2001), Acquisition, optimization and interpretation of X-
847 ray computed tomographic imagery: applications to the geosciences, *Computers &
848 Geosciences*, 27(4), 381-400.

849 Keyes, S. D., K. R. Daly, N. J. Gostling, D. L. Jones, P. Talboys, B. R. Pinzer, R. Boardman,
850 I. Sinclair, A. Marchant, and T. Roose (2013), High resolution synchrotron imaging of wheat
851 root hairs growing in soil and image based modelling of phosphate uptake, *New Phytologist*,
852 198(4), 1023-1029.

853 Mooney, S. J. (2002), Three-dimensional visualization and quantification of soil macroporosity
854 and water flow patterns using computed tomography, *Soil Use and Management*, 18(2), 142-
855 151.

856 Mooney, S. J., and C. Morris (2008), A morphological approach to understanding preferential
857 flow using image analysis with dye tracers and X-ray Computed Tomography, *CATENA*, 73(2),
858 204-211.

859 Mooney, S. J., T. P. Pridmore, J. Helliwell, and M. J. Bennett (2012), Developing X-ray
860 Computed Tomography to non-invasively image 3-D root systems architecture in soil, *Plant
861 and Soil*, 352(1-2), 1-22.

862 Panfilov, M. (2000), *Macroscale models of flow through highly heterogeneous porous media*,
863 Springer.

864 Pavliotis, G., and A. Stuart (2008), *Multiscale Methods: Averaging and Homogenization*,
865 Springer.

866 Ramstad, T., P. E. Oren, and S. Bakke (2010), Simulation of Two-Phase Flow in Reservoir
867 Rocks Using a Lattice Boltzmann Method, *Spe Journal*, 15(4), 923-933.

868 Reinhart, K. G. (1961), The Problem of Stones in Soil-Moisture Measurement1, *Soil Sci. Soc.
869 Am. J.*, 25(4), 268-270.

870 Rogasik, H., J. W. Crawford, O. Wendroth, I. M. Young, M. Joschko, and K. Ritz (1999),
871 Discrimination of soil phases by dual energy x-ray tomography, *Soil Science Society of
872 America Journal*, 63(4), 741-751.

873 Rowell, D. L. (1994), *Soil science : methods and applications* Longman Scientific & Technical
874 ; Prentice Hall.

875 Taylor, H. M., M. G. Huck, B. Klepper, and Z. F. Lund (1970), Measurement of Soil-grown
876 Roots in a Rhizotron, *Agron. J.*, 62(6), 807-809.

877 Tippkötter, R., T. Eickhorst, H. Taubner, B. Gredner, and G. Rademaker (2009), Detection of
878 soil water in macropores of undisturbed soil using microfocus X-ray tube computerized
879 tomography (μ CT), *Soil and Tillage Research*, 105(1), 12-20.

880 Tucker, C. (2014), Reduction of air- and liquid water-filled soil pore space with freezing
881 explains high temperature sensitivity of soil respiration below 0 °C, *Soil Biology and*
882 *Biochemistry*, 78(0), 90-96.
883 van Genuchten, M. T. (1980), A Closed-form Equation for Predicting the Hydraulic
884 Conductivity of Unsaturated Soils¹, *Soil Sci. Soc. Am. J.*, 44(5), 892-898.
885 Wildenschild, D., J. W. Hopmans, M. L. Rivers, and A. J. R. Kent (2005), Quantitative
886 Analysis of Flow Processes in a Sand Using Synchrotron-Based X-ray Microtomography,
887 *Vadose Zone J.*, 4(1), 112-126.
888 Wildenschild, D., C. M. P. Vaz, M. L. Rivers, D. Rikard, and B. S. B. Christensen (2002),
889 Using X-ray computed tomography in hydrology: systems, resolutions, and limitations,
890 *Journal of Hydrology*, 267(3-4), 285-297.
891 Zappala, S., J. R. Helliwell, S. R. Tracy, S. Mairhofer, C. J. Sturrock, T. Pridmore, M. Bennett,
892 and S. J. Mooney (2013), Effects of X-Ray Dose On Rhizosphere Studies Using X-Ray
893 Computed Tomography, *PLoS ONE*, 8(6), e67250.

894

895

896

897 **8. Figures**

898 **Figure 1.** Outline of steps used in the subsampling, meshing and solution of cell
899 problem. Figures (a) and (b) show the subsampling of a 1.2 mm side length cube of the
900 segmented .stl file. Figure (c) shows the mesh generation. Figures (d) and (e) show the
901 generation of a truly periodic geometry through translation (d) and reflection (e), the original
902 volume mesh is shown in a lighter shade. Figure (f) shows the numerical solution for the local
903 velocity magnitude in the subsampled soil.

904

905 **Figure 2.** Water release characteristic of the sand and clay sieved (a) and field structured (b)
906 soils fitted to the van Genuchten (VG) curve. Error bars associated with histograms show one
907 standard deviation. Note the different scaling on the y axis for figures (a) and (b).

908

909 **Figure 3.** Greyscale images showing examples of field structured (a) & (b) and sieved (c) &
910 (d) clay (a) & (c) sand soil (b) & (d) at -75 kPa. Scale bar = 0.25 mm.

911

912 **Figure 4.** Hydraulic conductivity of field structured sand and clay soils averaged over all
913 directions for decreasing j corresponding to increasing volume. The dots show the result from
914 each of the cubic volumes, the lines show the average. The corresponding saturated hydraulic
915 conductivity measured for the sand and clay soils are $1.3 \times 10^{-3} \text{ cm s}^{-1}$ and $0.4 \times$
916 $10^{-3} \text{ cm s}^{-1}$ respectively.

917

Deleted: s

919 **Figure 5.** Hydraulic conductivity of field structured sand and clay soils as a function of
920 matric potential.

921 **Figure 6.** 3D core section of a sand (a) and clay (b) soil sample at the specific matric potentials
922 from saturation (left) to drier (right). Segmented phases are coloured brown (soil), blue (water
923 filled pores) and black (air filled pores). Scale bar = 5 mm.

924

925 **Figure 7.** 3D pore thickness heat maps for a representative sand (a-c) and clay (e-f) sample at
926 0 (a, d), -20 (b, e) and -75 (c, f) kPa. (g) total air filled pore volume (bars) and average individual
927 pore volumes (lines) for sand and clay soil. Error bars associated with histograms show one
928 standard deviation.

929

930

931

932

933

934

935

936

937

938

939

940

941

942 **Figure 1.**

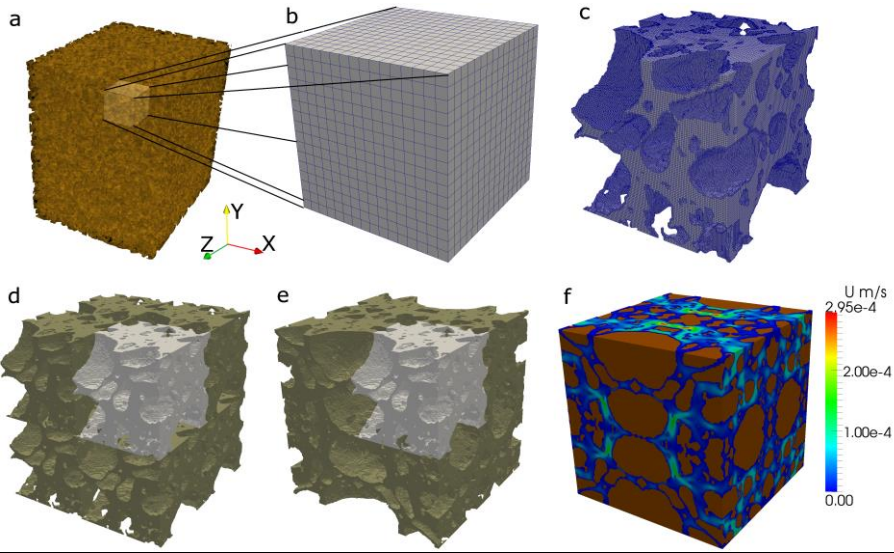
Deleted: ¶

Deleted: ¶

Page Break

¶

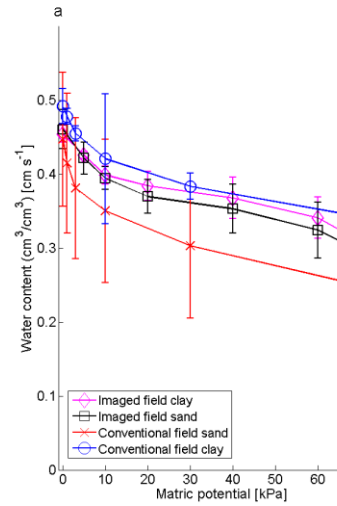
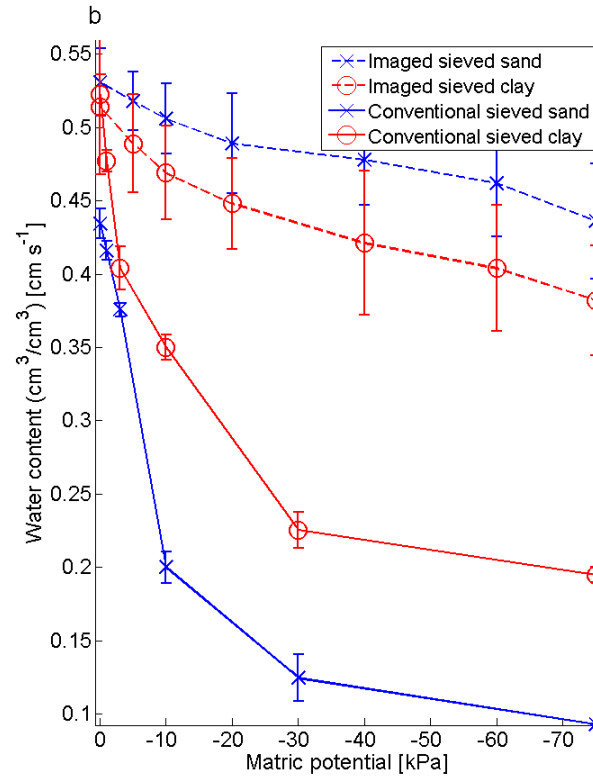
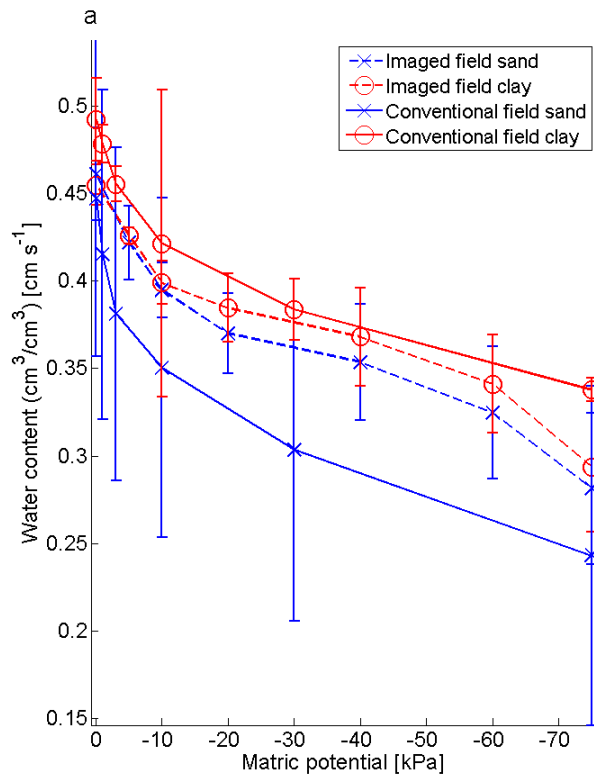
947



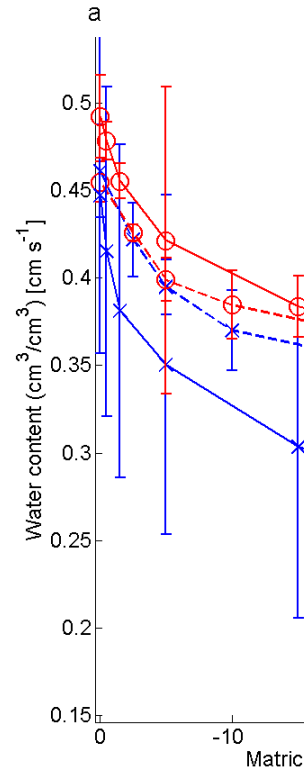
948

949
950
951

Figure 2.



Deleted:



Deleted:

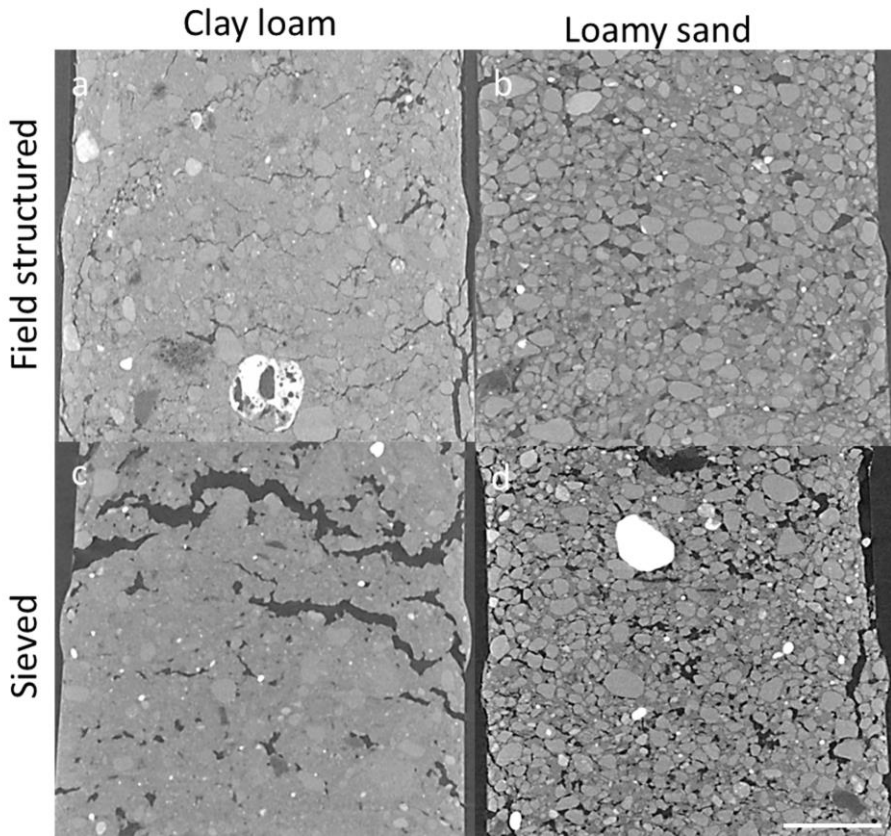
952

957

Deleted: ¶

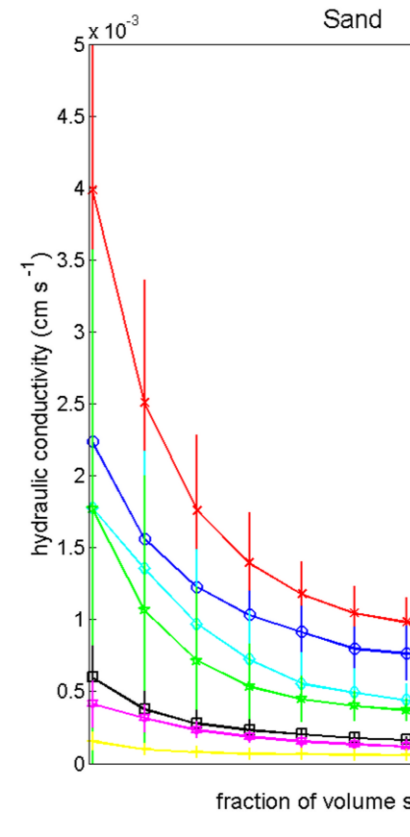
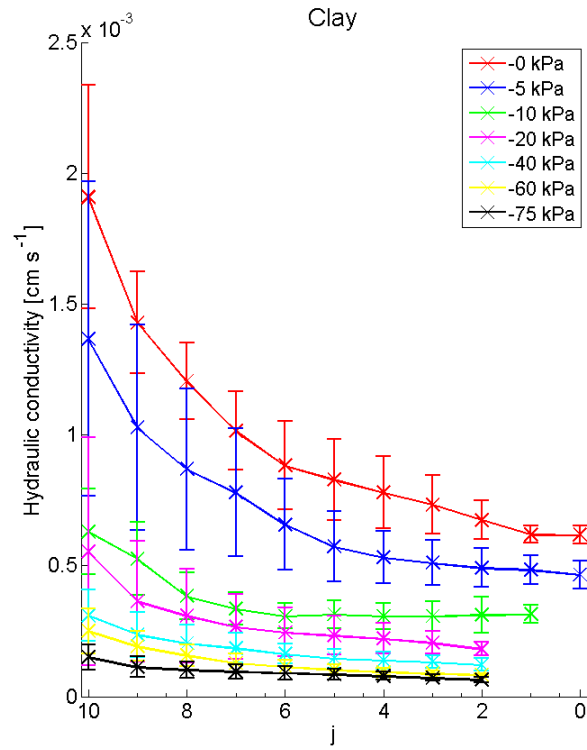
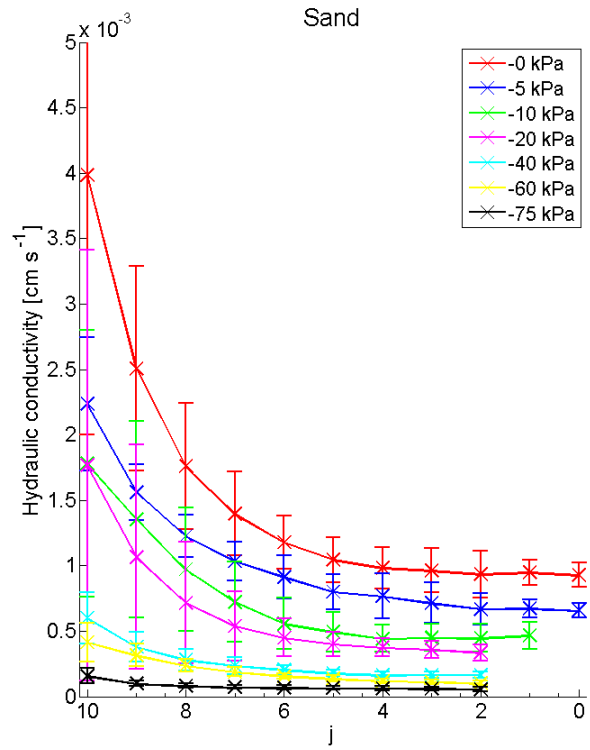
Deleted: ¶

960 **Figure 3.**
961



962
963
964
965
966
967
968
969
970

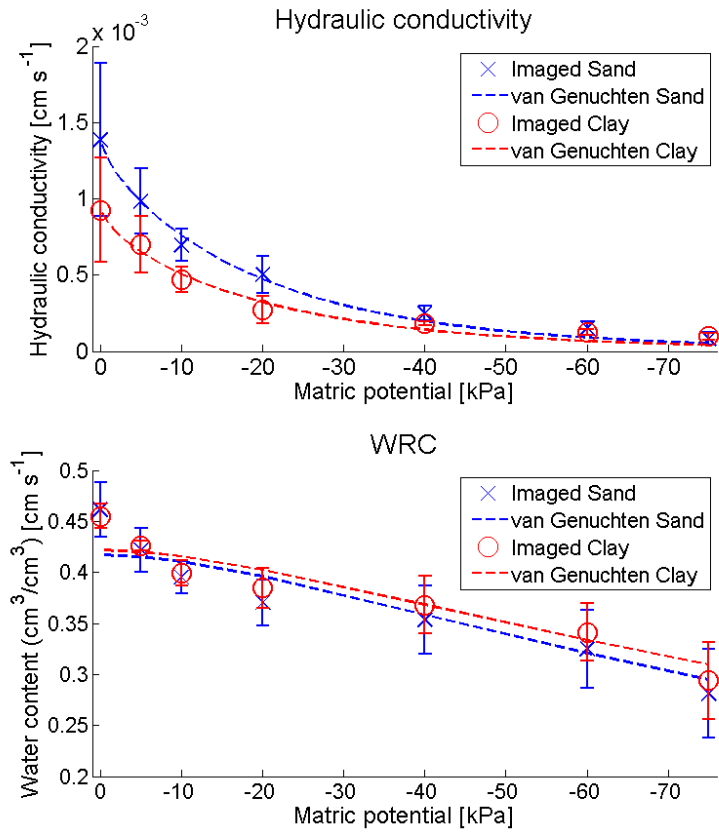
971 **Figure 4.**
 972



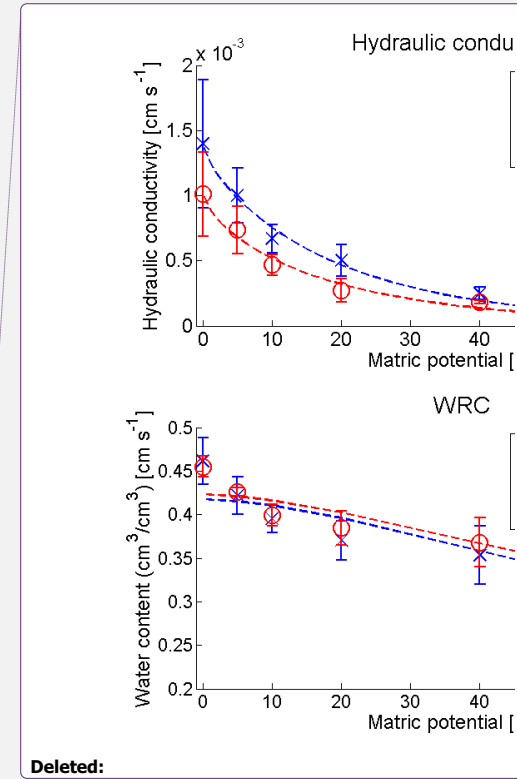
Deleted:

973
 974

976 **Figure 5.**



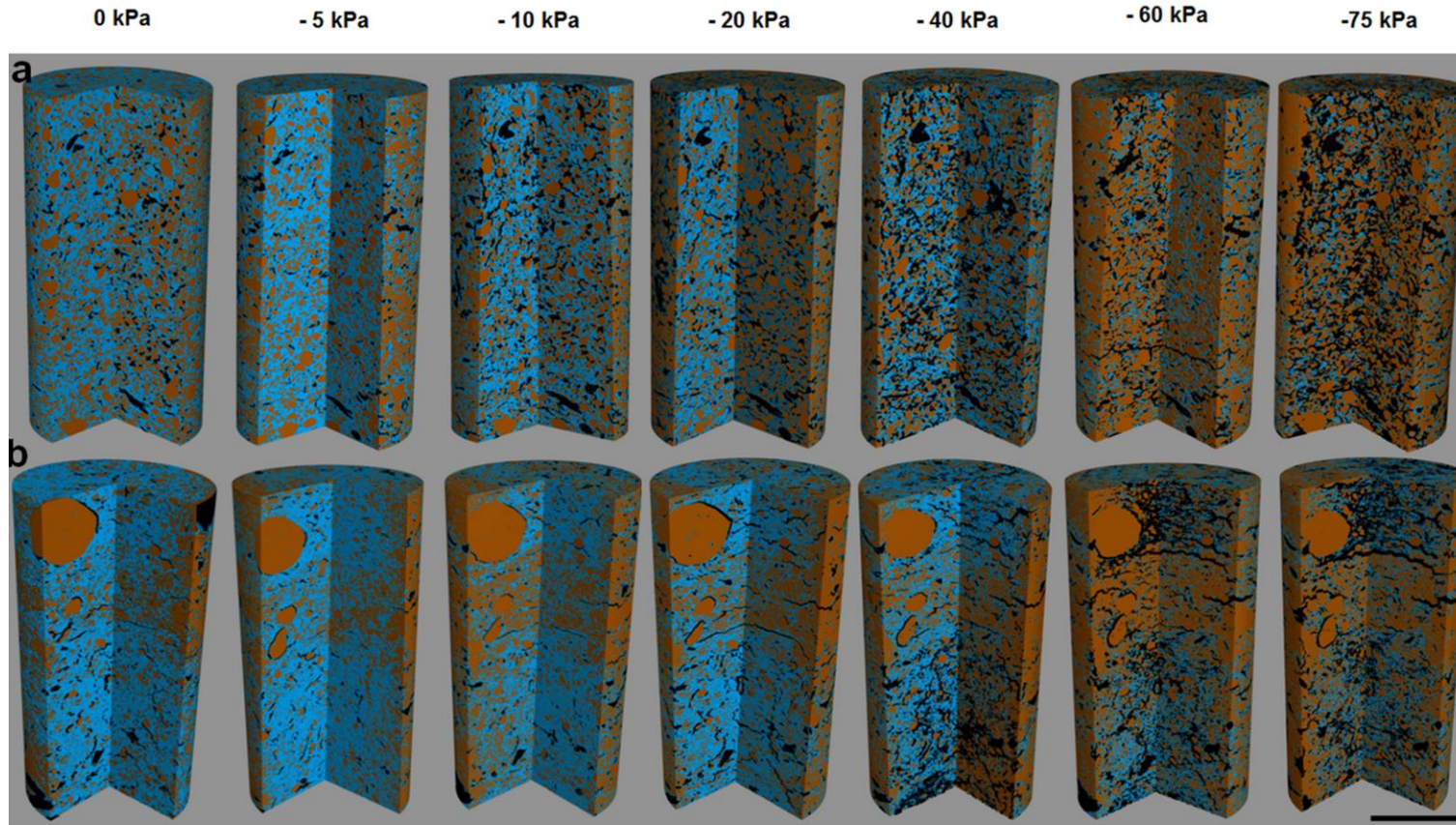
977



979

Figure 6.

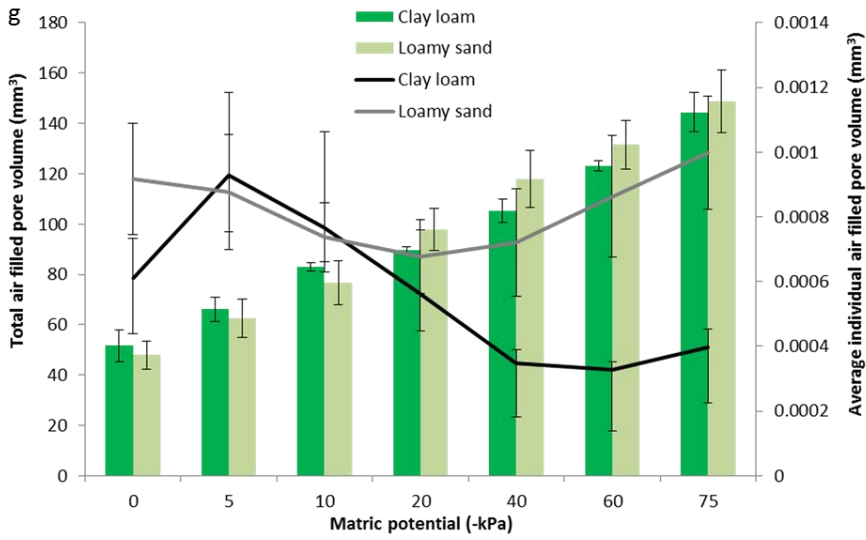
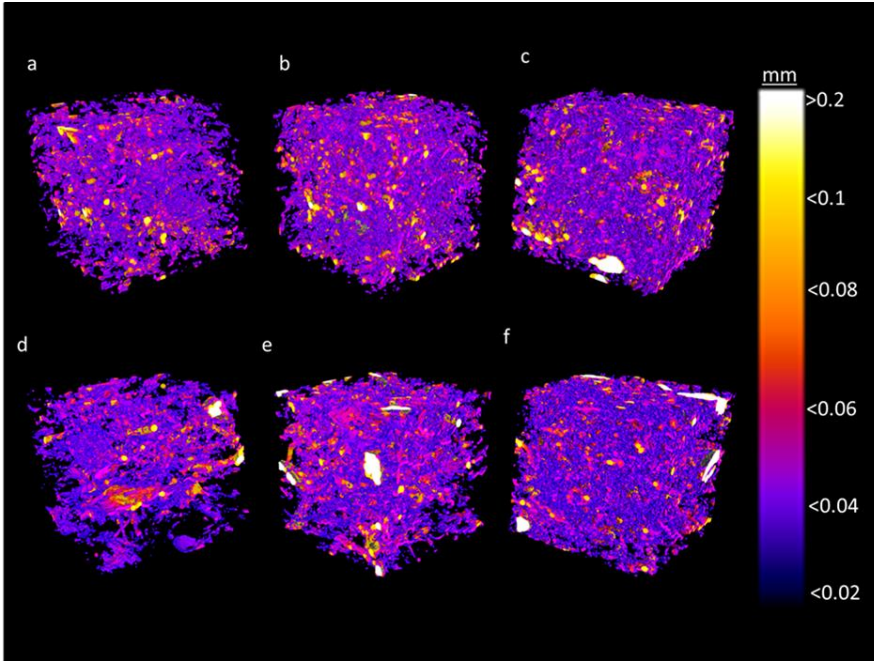
Deleted: ¶
¶



980

981

984 **Figure 7.**



985

986

Deleted: Section Break (Next Page)
 Formatted: Normal, No bullets or numbering
 Formatted: Font: Bold